Contents lists available at ScienceDirect

Organic Electronics

journal homepage: http://ees.elsevier.com

Optimization of gate-bias stability and gas-sensing properties of triethylsilylethynyl anthradithiophene micro-strip field-effect transistors by incorporating insulating polymer

Do Hun Kwak [a], Hyun Ho Choi [b], John E. Anthony [c], Seunghyun Kim [a], Hui Jeong Chae [a], Jinhyun Hwang [a], Shichoon Lee [d], Hui Joon Park [e], Bong-Gi Kim [a,f], Wi Hyoung Lee [a,f,*]

[a] Department of Organic and Nano System Engineering, Konkuk University, Seoul, 05029, Republic of Korea
[b] School of Materials Science and Engineering, Gyeongsang National University, Jinju, 52828, Republic of Korea
[c] Center for Applied Energy Research, University of Kentucky, Lexington, 40511, USA
[d] Department of Aero-Materials Engineering, Jungwon University, Goesan, 28023, Republic of Korea
[e] Department of Organic and Nano Engineering, Hanyang University, Seoul, 04763, Republic of Korea
[f] Division of Chemical Engineering, Konkuk University, Seoul, 05029, Republic of Korea

ARTICLE INFO

Keywords
5,11-bis(triethylsilylethynyl)anthradithiophene
Gate-bias stability
Organic field-effect transistor
Gas-sensing properties
Insulating polymer
Micro-strip

ABSTRACT

The control of the microstructure and patterning of 5,11-bis(triethylsilylethynyl)anthradithiophene (TES-ADT) film is essential for high-performance TES-ADT field-effect transistors (FETs) as a NO_2 gas sensor. In this study, a binary blend film based on TES-ADT and insulating polymer was annealed by solvent vapor with patterned PDMS molds. The solvent-containing PDMS mold led to the TES-ADT crystallization under the phase-separation between TES-ADT and PMMA. This resulted in highly crystalline micro-strip films where TES-ADT and the insulating polymer were phase-separated on top and bottom, respectively. The micro-strip structures can have superior gas sensor performance because they have additional gas diffusion paths compared to non-patterned structures. Initial investigations to clarify morphology and microstructure of the films revealed that lateral phase separation got dominant with increasing the portion of the insulating polymer. The blended films were then used as the active layer in the FET-based gas sensors. The use of blended films instead of non-blended TES-ADT film in FETs is advantageous in reducing both the threshold voltage and subthreshold slope while compromising the field-effect mobility. The sensing response as the gas sensors is slightly lower in the blended TES-ADT FET than in the non-blended TES-ADT FET. However, the utilization of blended films significantly enhanced the bias-stress stability. Accordingly, a uniform baseline of the sensor performance was achieved in TES-ADT: insulating polymer blended FETs. This trend was in contrast to an abrupt decrease in the sensing signals of the non-blended TES-ADT FETs. The enhanced bias stability of the blended FETs was exhibited as a result of covering the silanol groups in SiO_2 with a phase-separated insulating polymer. Our results provide a route for to the optimization of bias stability and response in TES-ADT micro-strip gas sensors through the application of a one-step blend technology.

1. Introduction

Gas sensors based on organic semiconductors have been studied extensively because the optical and electrical properties of organic semiconductors can be modulated by the adsorption or chemical reaction of target gas molecules [1–3]. Selective and sensitive detection of target gas molecules is required for the commercialization of organic semiconductor-based gas sensors [1,4–11]. The control of the interaction between organic semiconductors and gas molecules has been accomplished through molecular design, and several previous studies have reported the selective detection of harmful gases, i.e., volatile organic compounds (VOCs) through change in color in organic chromophore [12–15]. Because these VOCs are harmful to the human body [12,16], gas sensors with very high sensing response must be developed. In this regard, amperometric sensors, which monitor the change in current under gas exposure, are beneficial for quick detection. Typically, amperometric gas sensors based on organic semiconductors are constructed using an organic field-effect transistor (OFET) structure [1,7,17,18]. Because the intrinsic conductivity of organic semiconductors is lower

* Corresponding author. Department of Organic and Nano System Engineering, Konkuk University, Seoul, 05029, Republic of Korea.
E-mail address: whlee78@konkuk.ac.kr (W.H. Lee)

https://doi.org/10.1016/j.orgel.2020.105878
Received 28 February 2020; Received in revised form 8 June 2020; Accepted 18 June 2020
Available online xxx
1566-1199/

than those of carbon or inorganic semiconductors, the current signal must be amplified to obtain a significant change in current for gas sensor applications [19]. Fortunately, in field-effect transistors (FETs), gate bias can amplify the source-drain current through the accumulation of charge carriers under the gate-induced polarization of the dielectric [20–22]. This approach is significantly different from gas sensors based on inorganic semiconductors, where the change in current under gas exposure is monitored without applying gate bias.

Although gate bias can modulate the level of source-drain current in OFETs, continuous gate bias typically leads to instability in device performance [23,24]. The most common phenomenon of bias instability occurs as a decrease in the source-drain current induced by threshold voltage shift [25]. Trapping of charge carriers at the semiconductor, semiconductor-dielectric interface, and dielectric screens the applied gate-bias, thereby leading to the shift in threshold voltage and decrease in source-drain current. Thus, much higher gate-bias must be loaded on FET to compensate for the decrease in current. In this regard, a gate-bias must be applied in operating the OFET gas sensor. However, a gate bias applied to the device is accompanied by a decrease in the amount of current, causing a change in the base current of the sensor. Therefore, it is vital to reduce the bias-stress instability in this gas sensor type in developing a stable gas sensor without varying the base current. We noticed that incorporating an insulating polymer into an organic semiconductor has been investigated to enhance gas-sensor performance [26]. However, all the previous studies focused on the control of morphologies and microstructures to increase the surface area for increased gas adsorption [27–30]. Thus, it is meaningful to optimize the bias stability and gas-sensing properties of OFET by applying one-step blend technology.

In this work, we used binary blend films based on 5,11-bis(triethylsilylethynyl)anthradithiophene (TES-ADT) and poly(methyl methacrylate) (PMMA) for the sensitive detection of NO_2 gas. The TES-ADT: PMMA blend films were patterned with engraved polydimethylsiloxane (PDMS) mold containing a solvent to increase the gas penetration pathway of TES-ADT. PDMS mold is effective in obtaining highly crystalline TES-ADT patterns, and the same method was employed to fabricate micro-strips of TES-ADT: PMMA blended films [31–33]. The micro-strip structures showed superior gas sensor performance because they have additional gas diffusion paths compared to non-patterned structures (Fig. S1 in Supplementary data). The PDMS mold led to the TES-ADT crystallization under the phase-separation between TES-ADT and PMMA. The morphological and microstructural characteristics of TES-ADT: PMMA micro-strips are extensively studied, and these properties are correlated with the electrical properties (i.e., gas sensing properties and bias stabilities) of OFET-based gas sensors.

2. Experimental section

2.1. Fabrication of TES-ADT: PMMA patterns and FETs

TES-ADT was synthesized according to the synthetic route followed by Anthony et al. [34], with support from the National Science Foundation under Cooperative Agreement No. 1849213. PMMA (molecular weight of 996 kDa) and all the solvents were purchased from Aldrich. An 1 wt% of TES-ADT:PMMA blend dissolved in toluene with different blend ratio (1:0, 1:0.2, 1:0.5, and 1:1) were spin-casted at ~1000 rpm for 60 s onto the SiO_2 (300 nm)/Si substrates, which were earlier cleaned with excess solvent and ultraviolet/ozone treatment for 30 min. As-spun TES-ADT: PMMA films were transferred to a hot plate at 95 °C and dried in a vacuum oven to remove excess residual solvent. A solvent-soaked PDMS mold with a pre-designed groove pattern was utilized to fabricate line patterns of the TES-ADT: PMMA films. The TES-ADT: PMMA line patterns were fabricated during contact of the solvent-soaked PDMS mold with the TES-ADT: PMMA films. The contact process was carried out under a mild pressure of ~3.5 kPa and the contact time was controlled to obtain the TES-ADT: PMMA line patterns with minimum residue at the contact region. Au source/drain electrodes were thermally deposited on the patterned TES-ADT: PMMA to fabricate bottom-gate/top contact FETs. The channel width was 455 μm, whereas the channel length was fixed at 100 μm.

2.2. Characterization of the blended films, FETs, and gas sensors

The morphologies of the TES-ADT: PMMA patterns were characterized using a polarized optical microscope (POM, Nikon) and an atomic force microscope (AFM, Park Scientific Instrument). The TES-ADT layer was selectively etched with *n*-hexane to access the phase-separation interface between TES-ADT and PMMA, and the interface was characterized using AFM. The electrical properties of the TES-ADT: PMMA FETs were measured with a Keithley semiconductor parameter analyzer connected with a vacuum probe station (MS TECH). Transfer curves were obtained at a fixed source-drain voltage (V_{DS} = −80 V) by sweeping the gate voltage (V_{GS}) from 40 to −80 V. Gas-sensing properties were measured by connecting the three FET electrodes to the sensor setup (PSS Korea) with an ultrathin Ag wire. Dynamic gas-sensing properties of the TES-ADT: PMMA FETs were monitored at a fixed V_{GS} of −20 V and V_{DS} of −10 V. The target NO_2 gas (30 ppm) and the pursing N_2 gas were periodically inserted into the gas chamber for 50 and 450 s, respectively. Gas-bias stability of the TES-ADT: PMMA FETs were measured at fixed V_{GS} = −20 V and V_{DS} = −10 V, where the source-drain current (I_{DS}) was recorded with time. The response rate and response were calculated and defined by the following equation:

$$Response = (I_a - I_b)/I_b \quad (1)$$

$$Response\ rate = (I_a - I_b)/I_b \times \frac{1}{t}\ [s^{-1}] \quad (2)$$

where I_a is the source-drain current after NO_2 injection, I_b is the source-drain current before NO_2 injection, and t is the NO_2 injection time.

3. Results and discussion

The fabrication procedure of the TES-ADT: PMMA micro-strip patterns in contact with the solvent-soaked PDMS mold is presented in Fig. 1. Solvent and contact time are critical parameters in successfully obtaining crystalline TES-ADT: PMMA patterns. The solubility of the solvent should match with TES-ADT and PMMA to obtain relief at the contact region. However, the crystallization of TES-ADT must be activated by solvent vapor annealing at the non-contact region. Solvent vapor provides enough mobility to the TES-ADT molecules and PMMA chains in the spin-cast TES-ADT: PMMA blended films, and thus, surface segregation of the TES-ADT molecules occurs owing to the differences in surface energy [35]. It must be noted that the water contact angle of a TES-ADT film is 104°, which is significantly higher than 70° for a PMMA film [36]. The crystallization of TES-ADT was then activated in a solvent vapor environment. Finally, highly crystalline TES-ADT: PMMA micro-strips were fabricated, as shown from the POM images (Fig. 2).

For the successive patterning of TES-ADT: PMMA, we found that 1.2-dichloroethane was the highly relevant solvent soaked in PDMS to minimize residue. The optimum contact time of the PDMS mold was 5 min. The shorter contact time is not relevant to the sufficient phase-separation and crystallization of the TES-ADT molecules. Conversely, longer contact times led to the dewetting of the TES-ADT crystals owing to the adverse effect of solvent vapor annealing. Incorporating PMMA resulted in the formation of a small quantity of residue at the removed area (Fig. 2b, c, and d), which is originated from the adhesive properties of PMMA chains. The methacrylate groups in PMMA inter-

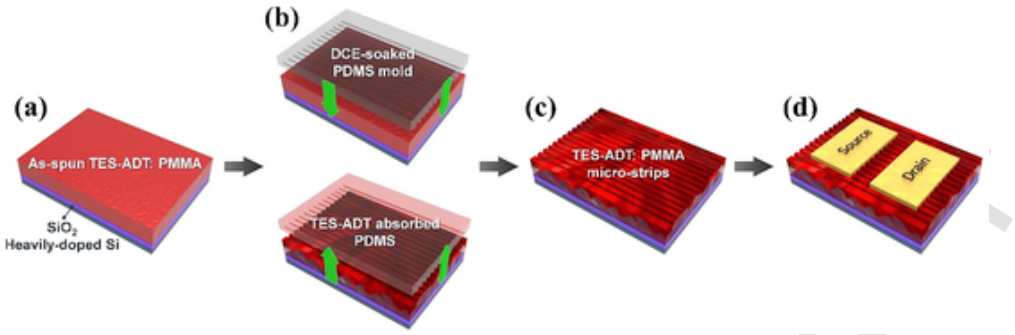

Fig. 1. Schematic illustration of the device fabrication process of TES-ADT: PMMA micro-strip patterns. (a) TES-ADT: PMMA film spin-casted onto UV ozone treated Si/SiO_2 substrate. (b, c) The TES-ADT film in contact with the PDMS mold was removed, while the TES-ADT crystals were formed in the non-contacted region. (d) The Au source/drain electrodes were thermally evaporated onto the TES-ADT: PMMA micro-strips, to fabricate the bottom-gate/top-contact FETs.

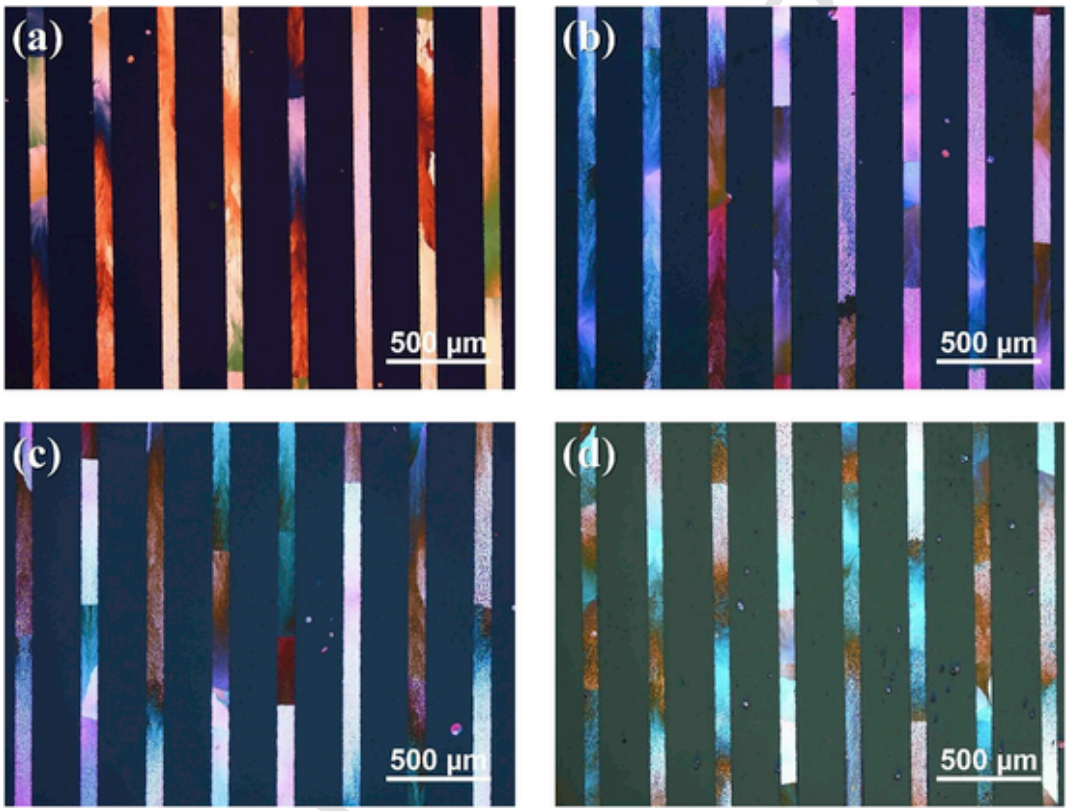

Fig. 2. POM images of the TES-ADT: PMMA blended films patterned from (a) pristine TES-ADT, (b) 1:0.2 TES-ADT: PMMA, (c) 1:0.5 TES-ADT: PMMA, and (d) 1:1 TES-ADT: PMMA.

act significantly with the hydroxyl groups in SiO_2, thereby prohibiting the detachment of the TES-ADT: PMMA film from the substrate.

Fig. 3 presents the surface and interface morphologies of the patterned TES-ADT: PMMA micro-strip arrays. When the pristine TES-ADT film was patterned with the PDMS mold, highly crystalline TES-ADT crystals with terraces and steps were detected (Fig. 3a). The solvent in the PDMS mold was vaporized, and these solvent molecules impart mobility to the crystallization in the confined line zones. When a small quantity of PMMA was added to the TES-ADT film, the TES-ADT molecules segregated at the air-film interface, as confirmed by the surface morphology of the crystalline TES-ADT (Fig. 3b top). However, PMMA was phase-separated at the bottom region of the blend film. The top TES-ADT layer was selectively etched with the *n*-hexane to determine the formation of the TES-ADT-top/PMMA-bottom structure. Fig. 3b (bottom) displays the underlying PMMA image of the 1:0.2 TES-ADT: PMMA blended film. A uniform PMMA layer was formed, except at some regions, which corresponded to the uncovered SiO_2 surface without PMMA. The thickness of the underlying PMMA layer was approximately 40 nm. When the mixing ratio of PMMA in the TES-ADT: PMMA blend was increased to 1:0.5, the intermixing of TES-ADT and PMMA prohibited the vertical phase separation between TES-ADT and PMMA (Fig. 3c top). In addition, the interface morphology of the TES-ADT: PMMA blend exhibited a bicontinuous morphology of PMMA (Fig. 3c bottom), which indicated that lateral phase separation also occurred during the phase separation and crystallization with the PDMS mold. When a 1:1 wt ratio of TES-ADT: PMMA blend was crystallized with the solvent-soaked PDMS mold, the phase-separation time was insufficient to enable the full segregation of TES-ADT at the top (Fig. 3d top). Accordingly, the morphology of the interface between TES-ADT and PMMA was rough, as confirmed by the bumpy image in the etched 1:1 TES-ADT: PMMA blended film (Fig. 3d bottom).

The electrical properties of FETs were measured after depositing Au source/drain electrodes onto the TES-ADT: PMMA micro-strips. Fig. 4 depicts the transfer characteristics of the TES-ADT: PMMA micro-

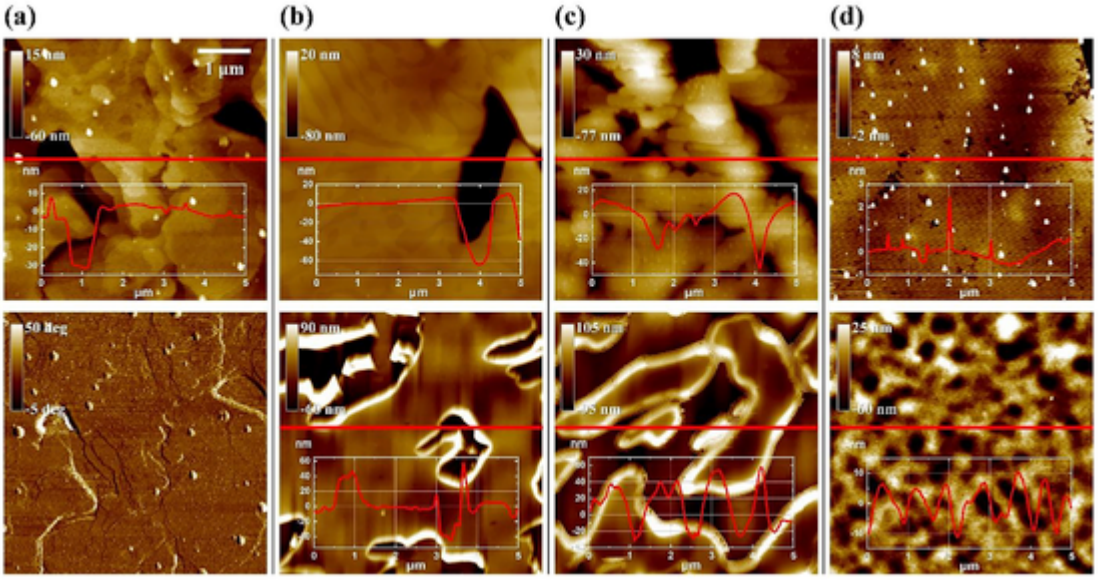

Fig. 3. AFM topographies of the patterned TES-ADT and TES-ADT: PMMA blended films: a) pristine TES-ADT (top: height image; bottom: phase image), b top) 1:0.2 TES-ADT: PMMA, c top) 1:0.5 TES-ADT: PMMA, d top) 1:1 TES-ADT: PMMA. The bottom images in b, c, and d show the interface morphologies after the TES-ADT layers were selectively etched with *n*-hexane. The red lines indicate the section profile for the height images. (For interpretation of the references to color in this figure legend, the reader is referred to the Web version of this article.)

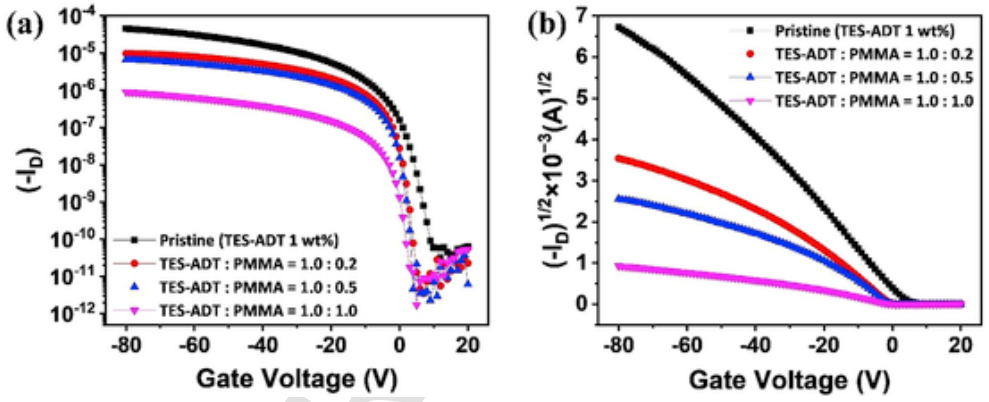

Fig. 4. Transfer characteristics of pristine TES-ADT and TES-ADT: PMMA blended FETs: (a) drain current versus V_{GS} and (b) square root of the drain current versus V_{GS}. V_{DS} was fixed at −80 V.

strip FETs with different blending ratios of PMMA. The device parameters including field-effect mobility (μ_{FET}), threshold voltage (V_{TH}), turn-on voltage (V_{ON}), on/off current ratio (I_{ON}/I_{OFF}), and subthreshold slope (SS), extracted from the transfer characteristics are summarized in Table 1. Note that the extracted field-effect mobilities did not include the effects of the underlying PMMA layer at the bottom, which provided an additional dielectric layer with a 300 nm-thick SiO_2 layer. Consequently, the calculated value might underestimate the μ_{FET} of FETs based on the TES-ADT: PMMA blends. Nonetheless, FETs with pristine TES-ADT micro-strips exhibited the highest on-current ratio and μ_{FET}. As the mixing ratio of PMMA in TES-ADT: PMMA micro-strips increased, the μ_{FET} decreased. It can be rationalized by the dilution effect of the incomplete vertical phase separation (Figs. 2 and 3). However, the incorporation of PMMA resulted in an abrupt decrease in the turn-on voltage V_{ON} (from 10 to 5 V) and off-state current, indicating that the addition of the insulating component into the organic semiconductor was beneficial in reducing the unintentional doping from atmospheric water and oxygen molecules. In addition, the subthreshold slope also decreased with the addition of insulating polymer (Table 1). Low subthreshold slope is advantageous in enhancing the switching speed of FETs. The addition of PMMA resulted in a low level of unintentional p-doping, which facilitated the rapid turn-on of the FETs. Fig. 5 pre-

Table 1
Electrical characteristics of OFETs based on pristine TES-ADT and TES-ADT: PMMA blended FETs.

OFET	μ_{FET} [cm^2/Vs]	V_{TH} [V]	V_{ON} [V]	I_{ON}/I_{OFF}	SS [V/dec]
Pristine (TES-ADT 1 wt%)	0.340 ± 0.067	−5 ± 0.25	10 ± 0.23	1.0×10^6	2.22 ± 0.071
TES-ADT: PMMA = 1.0:0.2	0.086 ± 0.013	0 ± 0.07	5 ± 0.08	1.0×10^6	1.78 ± 0.034
TES-ADT: PMMA = 1.0:0.5	0.058 ± 0.011	0 ± 0.04	5 ± 0.05	1.0×10^6	1.73 ± 0.036
TES-ADT: PMMA = 1.0:1.0	0.009 ± 0.002	0 ± 0.05	5 ± 0.04	1.0×10^5	1.74 ± 0.042

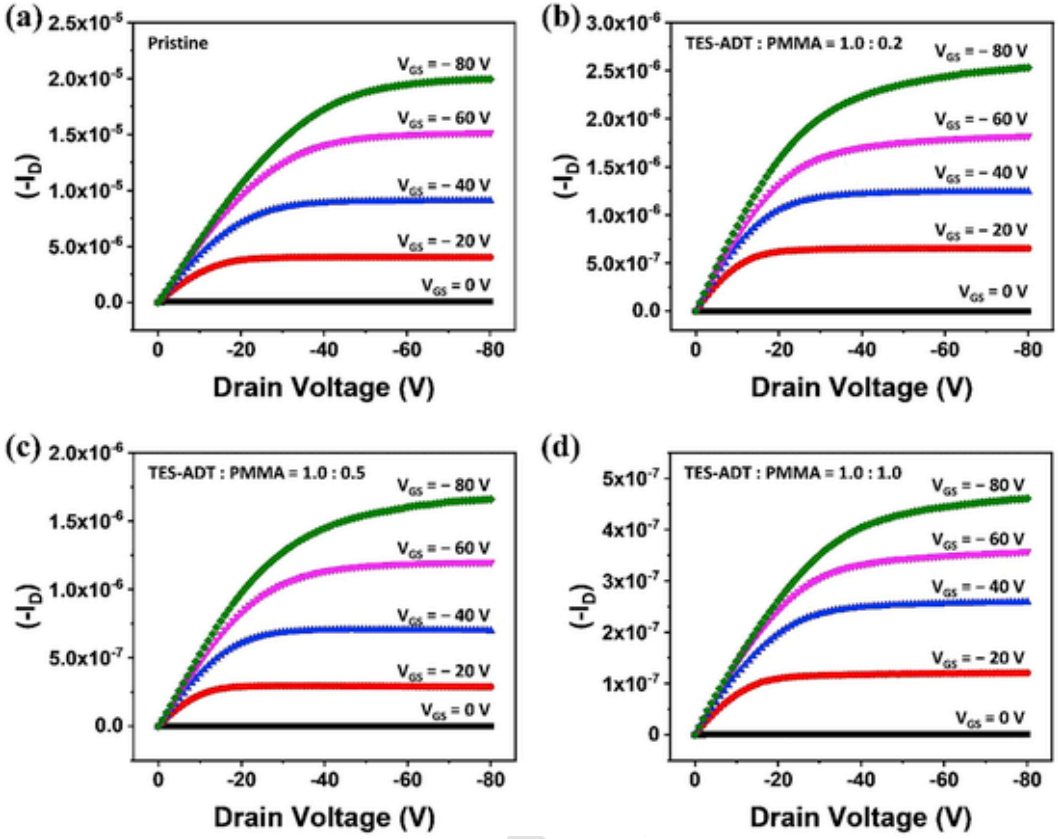

Fig. 5. Output characteristics of the pristine TES-ADT and TES-ADT: PMMA blended FETs: (a) pristine TES-ADT, (b) 1:0.2 TES-ADT: PMMA, (c) 1:0.5 TES-ADT: PMMA, and (d) 1:1 TES-ADT: PMMA.

sents the output characteristics of the FETs based on the TES-ADT and TES-ADT: PMMA blended micro-strips. All curves exhibit well-defined linear and saturation regions, demonstrating that the incorporation of PMMA in TES-ADT does not trigger any contact-related injection problems.

The gas sensing properties were measured using 30 ppm NO_2 as a target gas. NO_2 is a toxic gas, which is produced from the combustion of fossil fuels, such as petroleum and coal. A small amount of NO_2 within the range of a few tens of ppm causes harmful effects on the human respiratory system [37]. Thus, sensitive detection of NO_2 is essential in a public healthcare system. Fig. 6a presents the variations in the normalized I_{DS} on periodic exposure to NO_2 target gas and N_2 pursing gas with time. A V_{GS} of −20 V was applied to amplify the I_{DS}, while the current change was monitored at a V_{DS} of −10 V. The pristine TES-ADT gas sensor exhibited the highest increase in current on exposure to NO_2. An increase in current is directly related to the accumulation of hole carriers by NO_2 with electron-withdrawing characteristics. The extracted response rate and response are presented in Fig. 6b and arranged as follows: Pristine TES-ADT > TES-ADT: PMMA (1.0:0.2) > TES-ADT: PMMA (1.0:0.5) > TES-ADT: PMMA (1.0:1.0). This trend is explained by the combined effects of μ_{FET} (saturation region) and subthreshold slope (turn-on region). The detection speed of the sensor is directly related with μ_{FET} [38]. Therefore, the high μ_{FET} of 0.34 cm^2/V from the pristine TES-ADT FETs, which was four times higher than that of TES-ADT: PMMA (1.0:0.2), must be reflected in the response rate and response. However, all the sensors were measured at V_{GS} = −20 V and V_{DS} = −10 V, which was the intermediate region before the saturation of the current. Hence, the subthreshold slope relating to the switching speed for turning on/off must also be consid-

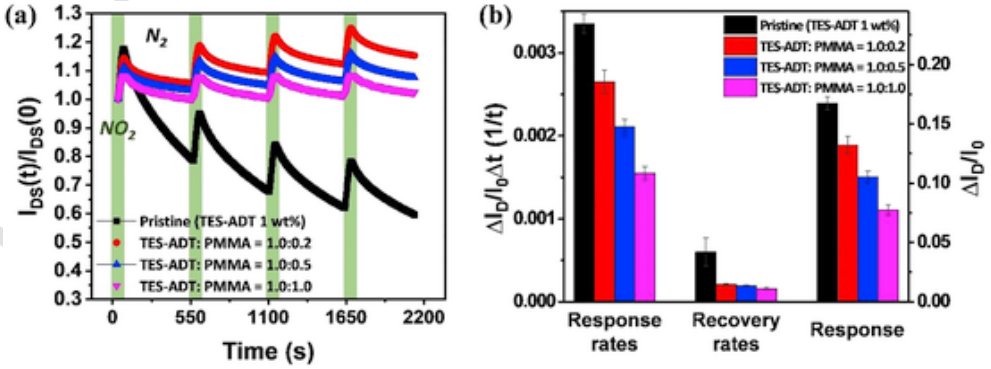

Fig. 6. Dynamic gas-sensing properties of an FET-based gas sensor with pristine TES-ADT and TES-ADT: PMMA blended films: (a) $I_D(t)/I_D(0)$ versus time curves for periodic exposure to 30 ppm NO_2. (b) Extracted sensing parameters of the pristine TES-ADT and TES-ADT: PMMA gas sensors. Left axis: Response/recovery rates; Right axis: Response. During the entire experimental tests, V_{GS} and V_{DS} were fixed at −20 and −10 V, respectively.

ered. The addition of PMMA resulted in a low subthreshold slope, which made up for the decrease in μ_{FET}. Fig. 6b presents the extracted sensing parameters of the TES-ADT and TES-ADT: PMMA blended FETs, which are summarized in Table 2.

The response rate and response of the TES-ADT: PMMA (1:0.2) blended FETs were only 26.5% lower than those of other TES-ADT FETs. We can ignore any morphological effects of the TES-ADT: PMMA (1:0.2) blended film on the sensor performance because TES-ADT was fully segregated at the surface for this mix ratio (Fig. 3b top). A further decrease in response with the addition of PMMA was related to the decrease in μ_{FET} due to the incomplete vertical phase separation between TES-ADT and PMMA. However, the recovery rates of the TES-ADT: PMMA blended FETs were approximately three times lower than those of TES-ADT FETs. The high recovery rate of TES-ADT FETs was caused by the high current decay (i.e., bias instability) under the sensor operation condition (V_{GS} = −20 V and V_{DS} = −10 V); therefore, the extracted recovery rate in the pristine TES-ADT sensor was overestimated.

Bias stabilities of the FETs were evaluated as a time-dependent parameter at the bias stress condition corresponding to the sensor operation condition to analyze the current decay behaviors of the TES-ADT and TES-ADT: PMMA micro-strip FETs (Fig. 7a). Fig. 7b presents the normalized current-decay curves of the FETs. TES-ADT FETs exhibited the worst bias-stress stability; only 40% of the current survived under continuous bias for 1 h. The resultant bias instability generally occurred owing to the charge trapping at the semiconductor (TES-ADT film), semiconductor/dielectric interface (TES-ADT/SiO_2 interface), and gate-dielectric (SiO_2), and source-drain contacts [39–43]. Table 3 presents the extracted characteristic time (τ) and dispersion parameter (β) by fitting the curves with the stretched exponential equation [24]. The characteristic time, which corresponded to the number of charge carriers in a mobile state, increased with the PMMA mixing ratio. Accordingly, the addition of PMMA significantly enhanced the bias-stress stability, which was beneficial for the accurate measurement of the gas molecules. It must be noted that the uniform baseline in sensor performance is essential for the commercialization of amperometric gas sensors. It was reported that the grain boundaries of TES-ADT films provide charge trapping sites for bias instability [44]. In this study, the density of the grain boundaries in the TES-ADT: PMMA blended films were not smaller than that of the pristine TES-ADT film (Fig. 2). Hence, there must be other reasons responsible for such enhancement of the bias stabilities. We noticed that the phase-separated PMMA layer at the bottom provides a surface modification layer of the SiO_2 dielectric. Thus, silanol groups at the SiO_2 surface were covered by the PMMA layer, preventing charge-trapping at the semiconductor/dielectric interface. We are unsure about the role of polar methacrylate groups in PMMA, which is useful in improving bias stability under the OFF-state bias (i.e., positive gate bias). We speculate that this effect was restricted in our ON-state bias experiments. Further studies are in progress to examine the effects of insulating polymers on the bias stabilities and gas-sensing properties of TES-ADT: insulating polymer FETs.

4. Conclusions

In this study, we optimized the gas-sensing properties of TES-ADT micro-strip FETs by incorporating PMMA. Solvent vapor annealing with PDMS molds enabled the fabrication of highly crystalline TES-ADT: PMMA micro-strip arrays. AFM analyses confirmed the vertical phase-separated structure, consisting of TES-ADT-top and PMMA-bottom layers. However, lateral phase separation also occurred, especially when the mix ratio of PMMA in the blended solution was high. Therefore, the increase in the PMMA mix ratio decreased the field-effect mobility of the TES-ADT: PMMA micro-strip FETs. The PMMA component, conversely, reduced both the turn-on voltage and the subthreshold slope by decreasing the unintentional doping from atmospheric water and oxygen molecules. The response rate and response of the TES-ADT micro-strip gas sensors were better than those of the TES-ADT: PMMA micro-strip gas sensors. The gate-bias stress during the sensor operation led to abrupt decrease in the current signal in the TES-ADT gas sensors. The TES-ADT: PMMA gas sensors, however, exhibited high gate-bias stability because the phase-separated PMMA layer at the bottom covered the hydroxyl groups in the SiO_2 dielectric. In our study, we proposed a method of optimizing the gate-bias stability and gas-sensing properties of TES-ADT FETs by adopting a polymer blend technology.

Table 2
Dynamic sensing properties of gas sensors based on the pristine TES-ADT and TES-ADT: PMMA blended FETs.

OFET-based gas sensor	Response rate [s^{-1}]	Recovery rate [s^{-1}]	Response
Pristine (TES-ADT 1 wt%)	0.00335 ± 0.00011	0.00060 ± 0.00017	0.167 ± 0.0057
TES-ADT: PMMA = 1.0:0.2	0.00265 ± 0.00014	0.00021 ± 0.000009	0.132 ± 0.0070
TES-ADT: PMMA = 1.0:0.5	0.00211 ± 0.00009	0.00019 ± 0.000005	0.106 ± 0.0046
TES-ADT: PMMA = 1.0:1.0	0.00155 ± 0.00008	0.00016 ± 0.000014	0.077 ± 0.0042

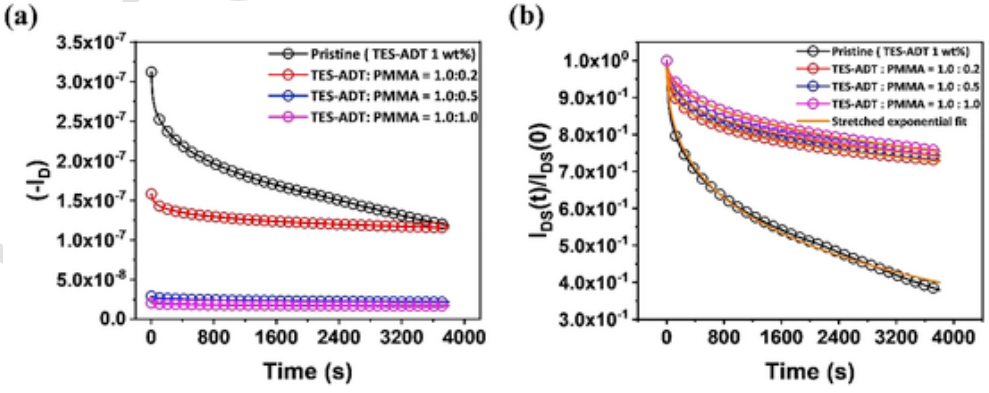

Fig. 7. Bias-stress stability curves of the pristine TES-ADT and TES-ADT: PMMA blended FETs: (a) drain current versus time, (b) $I_D(t)/I_D(0)$ versus time. V_{GS} = −20 V and V_{DS} = −10 V were continuously applied to the FETs.

Table 3
Extracted characteristic time (τ) and dispersion parameter (β) by fitting curves in Fig. 7b with the stretched exponential equation.

OFET-based gas sensor	τ [× 10^5 s]	β
Pristine (TES-ADT 1 wt%)	0.40	0.48
TES-ADT: PMMA = 1.0:0.2	1.51	0.31
TES-ADT: PMMA = 1.0:0.5	2.00	0.31
TES-ADT: PMMA = 1.0:1.0	6.85	0.31

Declaration of competing interest

The authors declare that they have no known competing financial interests or personal relationships that could have appeared to influence the work reported in this paper.

Acknowledgements

This paper was supported by Konkuk University in 2017.

Appendix A. Supplementary data

Supplementary data to this article can be found online at https://doi.org/10.1016/j.orgel.2020.105878.

References

[1] C Zhang, P Chen, W Hu, Organic field-effect transistor-based gas sensors, Chem. Soc. Rev. 44 (2015) 2087–2107.
[2] J T Mabeck, G G Malliaras, Chemical and biological sensors based on organic thin-film transistors, Anal. Bioanal. Chem. 384 (2006) 343–353.
[3] L Torsi, A Dodabalapur, L Sabbatini, P G Zambonin, Multi-parameter gas sensors based on organic thin-film-transistors, Sensor. Actuator. B Chem. 67 (2000) 312–316.
[4] H Fan, S Han, Z Song, J Yu, H E Katz, Organic field-effect transistor gas sensor based on GO/PMMA hybrid dielectric for the enhancement of sensitivity and selectivity to ammonia, Org. Electron. 67 (2019) 247–252.
[5] W Shi, J Yu, H E Katz, Sensitive and selective pentacene-guanine field-effect transistor sensing of nitrogen dioxide and interferent vapor analytes, Sensor. Actuator. B Chem. 254 (2018) 940–948.
[6] Y Seo, J H Lee, J E Anthony, K V Nguyen, Y H Kim, H W Jang, S Ko, Y Cho, W H Lee, Effects of grain boundary density on the gas sensing properties of triethylsilylethynyl-anthradithiophene field-effect transistors, Adv. Mater. Interfaces 5 (2018) 1701399.
[7] Y H Lee, M Jang, M Y Lee, O Y Kweon, J H Oh, Flexible field-effect transistor-type sensors based on conjugated molecules, Inside Chem. 3 (2017) 724–763.
[8] P Lienerth, S Fall, P Lévêque, U Soysal, T Heiser, Improving the selectivity to polar vapors of OFET-based sensors by using the transfer characteristics hysteresis response, Sensor. Actuator. B Chem. 225 (2016) 90–95.
[9] S Han, X Zhuang, W Shi, X Yang, L Li, J Yu, Poly(3-hexylthiophene)/polystyrene (P3HT/PS) blends based organic field-effect transistor ammonia gas sensor, Sensor. Actuator. B Chem. 225 (2016) 10–15.
[10] M Mirza, J Wang, L Wang, J He, C Jiang, Response enhancement mechanism of NO2 gas sensing in ultrathin pentacene field-effect transistors, Org. Electron. 24 (2015) 96–100.
[11] S Han, W Huang, W Shi, J Yu, Performance improvement of organic field-effect transistor ammonia gas sensor using ZnO/PMMA hybrid as dielectric layer, Sensor. Actuator. B Chem. 203 (2014) 9–16.
[12] Y Zhang, J Zhao, T Du, Z Zhu, J Zhang, Q Liu, A gas sensor array for the simultaneous detection of multiple VOCs, Sci. Rep. 7 (2017) 1960.
[13] A K Nayak, R Ghosh, S Santra, P K Guha, D Pradhan, Hierarchical nanostructured WO3–SnO2 for selective sensing of volatile organic compounds, Nanoscale 7 (2015) 12460–12473.
[14] T Rakshit, S Santra, I Manna, S K Ray, Enhanced sensitivity and selectivity of brush-like SnO2 nanowire/ZnO nanorod heterostructure based sensors for volatile organic compounds, RSC Adv. 4 (2014) 36749–36756.
[15] Z Wen, L Tian-mo, Gas-sensing properties of SnO2–TiO2-based sensor for volatile organic compound gas and its sensing mechanism, Phys. B Condens. Matter 405 (2010) 1345–1348.
[16] D Matatagui, O V Kolokoltsev, N Qureshi, E V Mejía-Uriarte, J M Saniger, A magnonic gas sensor based on magnetic nanoparticles, Nanoscale 7 (2015) 9607–9613.
[17] H Li, W Shi, J Song, H-J Jang, J Dailey, J Yu, H E Katz, Chemical and biomolecule sensing with organic field-effect transistors, Chem. Rev. 119 (2019) 3–35.
[18] D Elkington, N Cooling, W Belcher, P Dastoor, X Zhou, Organic thin-film transistor (OTFT)-Based sensors, Electronics 3 (2014) 234–254.
[19] C D Dimitrakopoulos, D J Mascaro, Organic thin-film transistors: a review of recent advances, IBM J. Res. Dev. 45 (2001) 11–27.
[20] N Karl, Charge carrier transport in organic semiconductors, Synth. Met. 133–134 (2003) 649–657.
[21] S Cherian, C Donley, D Mathine, L LaRussa, W Xia, N Armstrong, Effects of field dependent mobility and contact barriers on liquid crystalline phthalocyanine organic transistors, J. Appl. Phys. 96 (2004) 5638–5643.
[22] L Bürgi, T J Richards, R H Friend, H Sirringhaus, Close look at charge carrier injection in polymer field-effect transistors, J. Appl. Phys. 94 (2003) 6129–6137.
[23] R Häusermann, T Mathis, Gate bias stress in pentacene field-effect-transistors: charge trapping in the dielectric or semiconductor, Appl. Phys. Lett. 99 (2011).
[24] W H Lee, H H Choi, D H Kim, K Cho, 25th anniversary article: microstructure dependent bias stability of organic transistors, Adv. Mater. 26 (2014) 1660–1680.
[25] H Sirringhaus, Reliability of organic field-effect transistors, Adv. Mater. 21 (2009) 3859–3873.
[26] J H Lee, Y Seo, Y D Park, J E Anthony, D H Kwak, J A Lim, S Ko, H W Jang, K Cho, W H Lee, Effect of crystallization modes in TIPS-pentacene/insulating polymer blends on the gas sensing properties of organic field-effect transistors, Sci. Rep. 9 (2019) 21.
[27] S Hunter, J Chen, T D Anthopoulos, Microstructural control of charge transport in organic blend thin-film transistors, Adv. Funct. Mater. 24 (2014) 5969–5976.
[28] Y Diao, L Shaw, Z Bao, S C B Mannsfeld, Morphology control strategies for solution-processed organic semiconductor thin films, Energy Environ. Sci. 7 (2014) 2145–2159.
[29] H Dong, X Fu, J Liu, Z Wang, W Hu, 25th anniversary article: key points for high-mobility organic field-effect transistors, Adv. Mater. 25 (2013) 6158–6183.
[30] C Wang, H Dong, W Hu, Y Liu, D Zhu, Semiconducting π-conjugated systems in field-effect transistors: a material Odyssey of organic electronics, Chem. Rev. 112 (2012) 2208–2267.
[31] K V Nguyen, J H Lee, S C Lee, G M Ku, W H Lee, Simultaneous control of molecular orientation and patterning of small-molecule organic semiconductors for organic transistors, Org. Electron. 41 (2017) 107–113.
[32] D H Kwak, Y Seo, J E Anthony, S Kim, J Hur, H Chae, H J Park, B-G Kim, E Lee, S Ko, W H Lee, Enhanced gas sensing performance of organic field-effect transistors by modulating the dimensions of triethylsilylethynyl-anthradithiophene microcrystal arrays, Adv. Mater. Interfaces 7 (2020) 1901696.
[33] K Kim, M Jang, M Lee, T K An, J E Anthony, S H Kim, H Yang, C E Park, Unified film patterning and annealing of an organic semiconductor with micro-grooved wet stamps, J. Mater. Chem. C 4 (2016) 6996–7003.
[34] M M Payne, S R Parkin, J E Anthony, C-C Kuo, T N Jackson, Organic field-effect transistors from solution-deposited functionalized acenes with mobilities as high as 1 cm2/V·s, J. Am. Chem. Soc. 127 (2005) 4986–4987.
[35] W H Lee, J A Lim, D Kwak, J H Cho, H S Lee, H H Choi, K Cho, Semiconductor-dielectric blends: a facile all solution route to flexible all-organic transistors, Adv. Mater. 21 (2009) 4243–4248.
[36] S J Lee, Y-J Kim, S Y Yeo, E Lee, H S Lim, M Kim, Y-W Song, J Cho, J A Lim, Centro-apical self-organization of organic semiconductors in a line-printed organic semiconductor: polymer blend for one-step printing fabrication of organic field-effect transistors, Sci. Rep. 5 (2015) 14010.
[37] B Weinberger, D L Laskin, D E Heck, J D Laskin, The toxicology of inhaled nitric oxide, Toxicol. Sci. 59 (2001) 5–16.
[38] G Pfister, Hopping transport in a molecularly doped organic polymer, Phys. Rev. B 16 (1977) 3676–3687.
[39] M Tello, M Chiesa, C M Duffy, H Sirringhaus, Charge trapping in intergrain regions of pentacene thin film transistors, Adv. Funct. Mater. 18 (2008) 3907–3913.
[40] S G J Mathijssen, M Cölle, A J G Mank, M Kemerink, P A Bobbert, D M de Leeuw, Scanning Kelvin probe microscopy on organic field-effect transistors during gate bias stress, Appl. Phys. Lett. 90 (2007) 192104.
[41] S Yogev, R Matsubara, M Nakamura, Y Rosenwaks, Local charge accumulation and trapping in grain boundaries of pentacene thin film transistors, Org. Electron. 11 (2010) 1729–1735.
[42] K P Puntambekar, P V Pesavento, C D Frisbie, Surface potential profiling and contact resistance measurements on operating pentacene thin-film transistors by Kelvin probe force microscopy, Appl. Phys. Lett. 83 (2003) 5539–5541.
[43] C-H Kim, Bias-stress effects in diF-TES-ADT field-effect transistors, Solid State Electron. 153 (2019) 23–26.
[44] K V Nguyen, M M Payne, J E Anthony, J H Lee, E Song, B Kang, K Cho, W H Lee, Grain boundary induced bias instability in soluble Acene-based thin-film transistors, Sci. Rep. 6 (2016) 33224.